

Broadening of QSO Ly α forest absorbers

Tom Theuns¹, Joop Schaye² and Martin G. Haehnelt¹

¹ Max-Planck Institut für Astrophysik, Postfach 123, 85740 Garching, Germany

² Institute of Astronomy, Madingley Road, Cambridge CB3 0HA, UK

1 February 2008

ABSTRACT

We investigate the dependence of QSO Ly α absorption features on the temperature of the absorbing gas and on the amplitude of the underlying dark matter fluctuations. We use high-resolution hydrodynamic simulations in cold dark matter dominated cosmological models. In models with a hotter intergalactic medium (IGM), the increased temperature enhances the pressure gradients between low and high density regions and this changes the spatial distribution and the velocity field of the gas. Combined with more thermal broadening, this leads to significantly wider absorption features in hotter models. Cosmological models with little small scale power also have broader absorption features, because fluctuations on the scale of the Jeans length are still in the linear regime. Consequently, both the amplitude of dark matter fluctuations on small scales and thermal smoothing affect the flux decrement distribution in a similar way. However, the b -parameter distribution of Voigt profile fits, obtained by deblending the absorption features into a sum of thermally broadened lines, is largely independent of the amount of small scale power, but does depend strongly on the IGM temperature. The same is true for the two-point function of the flux and for the flux power spectrum on small scales. These three flux statistics are thus sensitive probes of the temperature of the IGM. We compare them computed for our models and obtained from a HIRES spectrum of the quasar Q1422+231 and conclude that the IGM temperature at $z \sim 3.25$ is fairly high, $T_0 \gtrsim 15000\text{K}$. The flux decrement distribution of the observed spectrum is fitted well by that of a ΛCDM model with that temperature.

Key words: cosmology: theory – intergalactic medium – hydrodynamics – large-scale structure of universe – quasars: absorption lines

1 INTRODUCTION

Neutral hydrogen in the intergalactic medium (IGM) produces a ‘forest’ of Ly α absorption lines bluewards of the Ly α emission line in quasar spectra (Bahcall & Salpeter 1965, Gunn & Peterson 1965). The general properties of these Ly α absorption lines are remarkably well reproduced in hydrodynamic simulations of cold dark matter (CDM) dominated cosmologies (Cen et al. 1994, Zhang, Anninos & Norman 1995, Miralda-Escudé et al. 1996, Hernquist et al. 1996, Wadsley & Bond 1996, Zhang et al. 1997, Theuns et al. 1998). In these simulations, intergalactic gas settles into the potential wells of CDM dominated sheets and filaments, aptly termed the cosmic web (Bond, Kofman & Pogosyan 1996). These large-scale density fluctuations in the intergalactic gas are responsible for the weak absorption lines of column density $N_{\text{HI}} \leq 10^{14.5}\text{cm}^{-2}$.

In the simulations, the typical widths of the peaks in the neutral hydrogen density, which occur when a line-of-sight crosses a sheet or filament, depend on the amplitude of dark matter fluctuations on small scales and by the smooth-

ing of these small scale fluctuations by gas pressure (‘Jeans smoothing’, e.g. Bryan et al. 1999). The widths of the absorption troughs are then determined by differential Hubble flow across the spatially extended absorber (Hernquist et al. 1996), peculiar velocities (Hui 1999), and thermal broadening.

Widths of absorption features have traditionally been characterized by the b -parameter distribution of Voigt profile fits, obtained by deblending the absorption features into a sum of discrete absorption lines. Recent high-resolution simulations have shown that these absorption lines in a standard CDM cosmology have b -parameters substantially narrower than observed in high-resolution Keck spectra (Theuns et al. 1998, Bryan et al. 1999). Since the b -parameters have been demonstrated to be at least partially thermally broadened (Haehnelt & Steinmetz 1998, Theuns et al. 1998, Hui & Rutledge 1999, Schaye et al. 1999a), Theuns et al. suggested that an increased temperature of the IGM might resolve the discrepancy.

At the relevant redshifts ($2 \lesssim z \lesssim 5$), the temperature of the low density IGM is determined by the interplay be-

tween adiabatic cooling and photoheating, which introduces a tight relation between density and temperature which can be well approximated by a power law (Hui & Gnedin 1997). Schaye et al. (1999a) used numerical simulations to demonstrate that the observed cut-off in the Doppler parameter distribution and its dependence on column density is the result of this $\rho - T$ relation. The exact form of the relation depends on the history of reionization and on cosmological parameters (Miralda-Escudé & Rees 1994, Hui & Gnedin 1997). For a given reionization history, higher temperatures are obtained for models with a higher baryon density $\Omega_b h^2$ and a smaller expansion rate of the Universe. Theuns et al. (1999) confirmed that in a model with high baryon density $\Omega_b h^2 = 0.025^*$, low matter density $\Omega_m = 0.3$ and $h = 0.65$ the b -distribution of the simulated absorption lines fits the observed distribution significantly better than for the colder standard CDM model.

However, the value of $\Omega_b h^2$ required is higher than the current best estimates $\Omega_b h^2 = 0.019$ (Burles & Tytler 1998) and it was suggested that additional heat sources neglected so far in the numerical simulations might contribute significantly to the heating rate. These include the photo electric heating by dust grains (Nath, Sethi & Shchekinov 1999) and Compton heating by the hard X-ray background (Madau & Efstathiou 1999). Alternatively, Abel & Haehnelt (1999) pointed out that the optically thin limit for the HeII photoheating rate usually assumed in these simulations might lead to an underestimate compared to the actual HeII photoheating rate by a factor of $\sim 2 - 3$.

Here we use high resolution hydrodynamic simulations to investigate how the IGM temperature and the amplitude of dark matter fluctuations affect the distribution of the gas and influences the widths of absorption features. The effect of different heating rates and the influence of the amplitude of dark matter fluctuations on the gas distribution are discussed in Section 3. In Section 4 we investigate the relative importance of the three thermal smoothing effects, Jeans smoothing, peculiar velocities and thermal broadening, and the amplitude of the dark matter fluctuations on the b -parameter distribution obtained by Voigt profile fitting. In Section 5 we discuss the effects on the one- and two-point function of the flux and on the flux power spectrum. Section 6 contains our conclusions. As the preparation of this paper was in its final stages a preprint by Bryan & Machacek (1999) was circulated that investigates some of the same issues.

2 SIMULATION PARAMETERS AND PREPARATION OF MOCK SPECTRA

We have simulated several different models, characterized by their total matter density Ω_m , the value of the cosmological constant Ω_Λ , the rms of mass fluctuations in spheres of $8h^{-1}$ Mpc, σ_8 and the heating rate. The parameters for these models are summarized in Table 1. All these models have $\Omega_m + \Omega_\Lambda = 1$. For our reference model L1 we take the currently favoured values $h = 0.65$ (see Freedman et al. 1998), $\Omega_b h^2 = 0.019$ (Burles and Tytler 1998),

* We write the present day Hubble constant as $H_0 = 100h$ km s $^{-1}$ Mpc $^{-1}$

Table 1. Models simulated

Name	Ω_m	h	σ_8	ϵ_{He}	X-ray	$\log T_0$	A
L0.3	0.3	0.65	0.9	HM/3	no	3.93	1.07
L1	0.3	0.65	0.9	HM	no	4.07	0.92
L2	0.3	0.65	0.9	2xHM	no	4.19	0.78
L3	0.3	0.65	0.9	3xHM	no	4.26	0.68
L1 σ .65	0.3	0.65	0.65	HM	no	4.07	1.05
L1 σ .4	0.3	0.65	0.4	HM	no	4.07	1.25
L3b	0.3	0.65	0.9	3xHM	no	4.26	0.59
LX	0.3	0.65	0.9	HM	yes	4.14	0.81
S3	1.0	0.50	0.5	3xHM	no	4.25	0.78

($\Omega_m, \Omega_\Lambda = (0.3, 0.7)$) (Efstathiou et al. 1999 and references therein), $\sigma_8 = 0.9$ (Eke, Cole & Frenk 1996) and a helium abundance of $Y = 0.24$ by mass. The IGM in this model is photoionized and photoheated by the UV-background from QSOs. The other models are variations on this set. Models L0.3, L2, L3, L3b and LX have the same normalization of the power spectrum as L1, but models L1 σ .65 and L1 σ .4 have smaller σ_8 . For the standard CDM model S3 we impose the normalization $\sigma_8 = 0.5$ deduced from the abundance of galaxy clusters (Eke, Cole & Frenk 1996). We have used CMBFAST (Seljak & Zaldarriaga 1996) to compute the appropriate linear matter transfer functions.

These simulations follow the evolution of a periodic, cubic region of the universe and are performed with a modified version of HYDRA (Couchman et al. 1995). HYDRA combines hierarchical P3M gravity (Couchman 1991) with smoothed particle hydrodynamics (SPH, Lucy 1977, Gingold & Monaghan 1977). One of us (TT) has parallelized this code for the Origin 2000 at DAMTP, Cambridge. These simulations use 64^3 particles of each species in a box of co-moving size $2.5h^{-1}$ Mpc, so the SPH particle masses are $1.14 \times 10^6 (h/0.65)^{-3} M_\odot$ and the CDM particles are more massive by a factor $\Omega_{\text{CDM}}/\Omega_b$. The gravitational softening length is 5 kpc. All our simulations were run with the same initial phases to minimize the effects of cosmic variance when comparing the different models. We have also run an additional model (L3b) which simulates a larger region ($5.0h^{-1}$ Mpc) with 128^3 particles of each type and thus the same numerical resolution as the other models. A simulation typically requires 1000-1500 steps to reach $z = 3$.

The detailed expressions for the heating and cooling rates as a function of temperature and ionizing flux are taken from Cen (1992) with some minor modifications (Theuns et al. 1998). We take the photoheating rate in the optically thin limit from Haardt & Madau (1996). This heating rate, denoted as ‘HM’ in the ϵ_{He} column of the Table, is imposed on models L1, L1 σ .65 and L1 σ .4. Models L2 and L3 are identical to L1, except that we have multiplied the helium photoheating rate by factors two and three respectively (keeping the ionization rate constant). Model L3b has the same heating rate as model L3. In model L0.3 we have reduced the helium photoheating by a factor 3. Model LX is identical to model L1, except that we have included Compton heating by the X-ray background as a function of redshift z at a rate (Madau & Efstathiou 1999)

$$\mathcal{H}_X(z) = 1.251 \times 10^{-31} (1+z)^{4.3} \exp(-(z/5)^2) n_e, \quad (1)$$

where \mathcal{H}_X is the heating rate in erg cm $^{-3}$ s $^{-1}$ and n_e is number density of free electrons in cm $^{-3}$. Finally, model

S3 is a standard CDM model, with the appropriate Haardt & Madau (1996) helium heating rate increased by a factor 3.

For each model we compute spectra along 1200 random lines of sight through the simulation box at a given redshift (usually $z = 3$) and then scale the ionizing background flux by the factor A in the analysis stage such as to give a chosen effective optical depth τ_{eff} . The factor A required to give $\tau_{\text{eff}} = 0.33$ at $z = 3$ is given in Table 1. We process these simulated spectra using the following procedure, designed to introduce the same biases as present in observational data from the HIRES spectrograph on the Keck telescope. Each spectrum is first convolved with a Gaussian with full width at half maximum of FWHM = 8 km s $^{-1}$ and re-sampled onto pixels of width 3 km s $^{-1}$. Photon and pixel noise is added such that the total signal-to-noise is 50. The ‘continuum’ of the spectra is then fitted with the method described in Theuns et al. (1998).

We also compare flux statistics for our simulated spectra to an observed HIRES spectrum of QSO 1422+231, kindly provided to us by W. Sargent and M. Rauch. The Ly α forest of this QSO extends over a significant redshift range, over which the effective optical depth evolves significantly. In addition, the signal-to-noise ratio varies as a function of wavelength and flux. We model these effects for this particular spectrum using the following detailed procedure (see also Rauch et al. 1997). We begin by dividing the spectrum in two halves. For each half, we take the simulation output at the appropriate redshift and scale the background flux such as to match the observed mean effective optical depth. We convolve the spectrum with a Gaussian with full width at half maximum of FWHM = 6.6 km s $^{-1}$ and re-sample it to pixels of the same size as the observed spectrum. We calculate the noise properties of the QSO spectrum as a function of flux and add Gaussian noise to the simulated spectra appropriate for the flux in each pixel. In the observed spectrum we exclude regions with identified metal absorption lines and the region close to the emission redshift which might be influenced by the proximity effect. Below we will show that this more elaborate procedure produces flux statistics in better agreement with the data than the simpler one described earlier. We use the same automated version of VPFIT (Carswell et al. 1987) to fit Voigt profiles to both simulated and observed spectra (see Theuns et al. 1998 for more details).

3 BROADENING OF QSO ABSORBERS

In this section we illustrate the effect of different broadening mechanisms on the widths of density peaks along a given line-of-sight. In particular, we discuss the relative importance of the three different thermal effects, namely Jeans smoothing, pressure-induced peculiar velocities and thermal broadening and compare these to the effect of the amplitude of dark matter fluctuations. In the following sections we will investigate how the different broadening mechanisms affect a number of different flux statistics.

3.1 Thermal smoothing

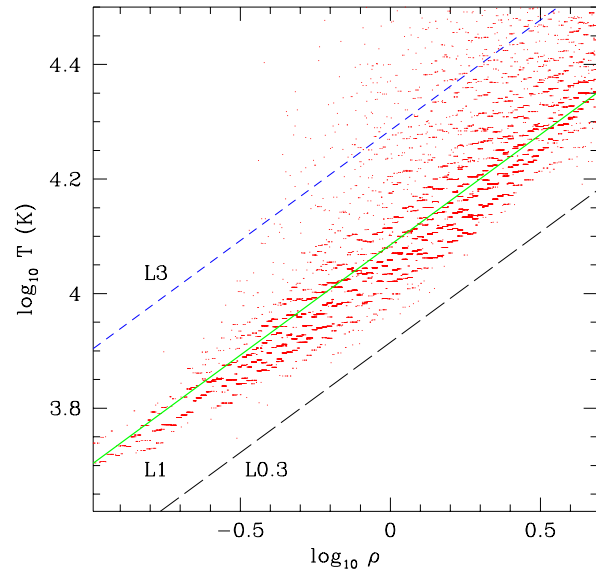


Figure 1. Temperature-density relation for model L1 (points) and a power-law fit (least absolute deviation; full line). Corresponding fits for models L3 (short dashed) and model L0.3 (long dashed) are shown for comparison. The ‘quantized’ appearance of the data points close to the full line is due to the usage of an interpolation scheme to compute temperatures.

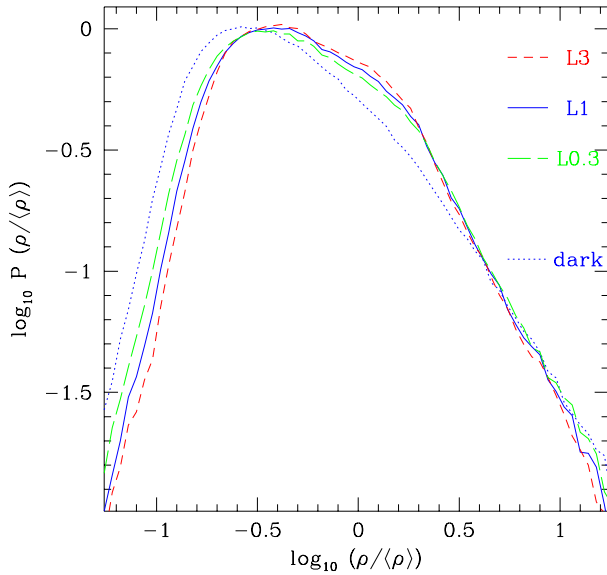


Figure 2. Volume weighted gas density probability distribution for models L0.3 (long dashed line), L1 (full line) and L3 (short dashed line). Dark matter distributions are indistinguishable for these models and are shown as the dotted line. Voids in the hotter model are less empty because of increased Jeans smoothing, and so a smaller fraction of the volume is occupied by very low density gas.

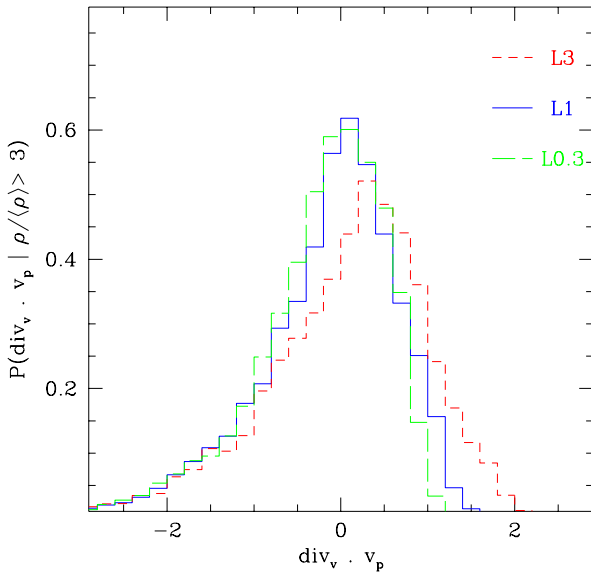


Figure 3. Probability distribution for the divergence of the peculiar velocity for models L0.3 (long dashed line), L1 (full line) and L3 (short dashed line). The larger pressure gradients in hotter models lead to more pronounced expansion of the gas out of potential wells.

3.1.1 The spatial distribution and the velocity of the gas

Figure 1 shows the temperature-density relations for the LCDM models where the HeII photo-heating is (0.3,1,3) times that in the optically thin limit, respectively. Over the interval shown, this relation is well approximated by a power law. The slope of this power law is determined by the reionization history (Hui & Gnedin 1997), which is the same for all models plotted here. The temperature T_0 at the mean density for $z = 3$ is also given in Table 1. As expected, T_0 increases with the heating rate as $T_0 \propto \epsilon_{\text{heat}}^{1/1.7}$ (Miralda-Escudé & Rees 1994).

In our models, baryons represent less than 15 per cent of the mass and increasing their temperature does not affect the dark matter distribution very much. In contrast, the gas distribution itself changes significantly as the temperature is raised, due to the larger pressure gradients that arise between high and low density regions. The increased pressure gradient forces the gas to settle into a configuration with a smaller density gradient in order to reach pressure equilibrium ($\nabla P/\rho = -\nabla\phi$), leading to broader structures. This effect is illustrated in Figure 2 where we plot the probability distribution function (PDF) of the gas density for the three models. Hotter models have a smoother density distribution with less empty voids and less gas at high density (and hence a narrower PDF), while the PDF of the DM density is unchanged. (Note that the shift between the PDFs of gas and DM shows explicitly that our simulations resolve the Jeans length.)

Another consequence of larger pressure gradients is that pressure-induced peculiar velocities in the gas become larger (see also Bryan et al. 1999). Figure 3 shows the PDF of the

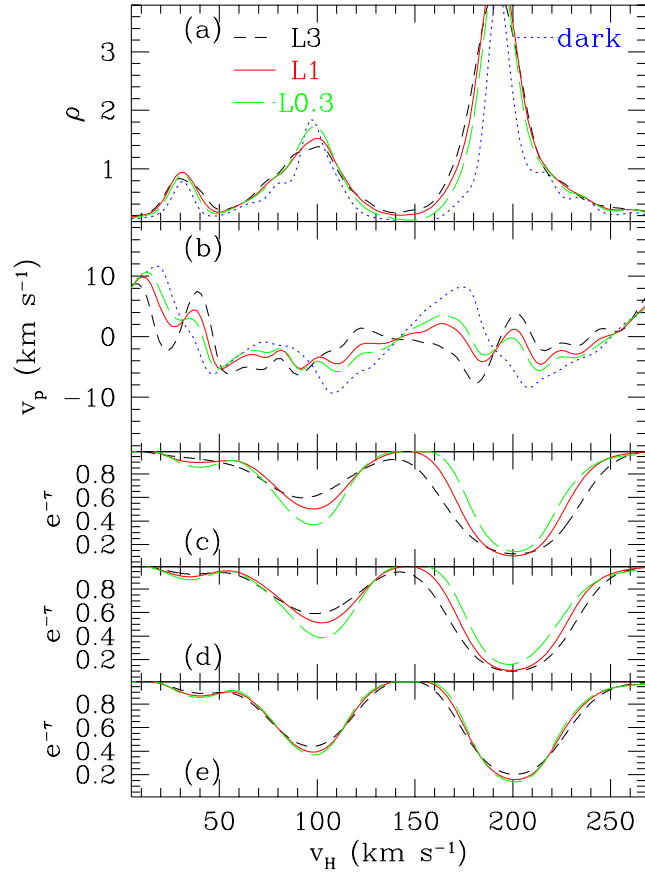


Figure 4. Top panels show the density and peculiar velocity along a sight line picked from the simulation, for models L0.3 (long dashed line), L1 (full line) and L3 (short dashed line). The dark matter profiles for these models are identical and are shown dotted. Panel (c) shows the corresponding spectra. Panel (d) shows spectra for the case where peculiar velocities are not included. Finally, panel (e) shows the spectrum for model L0.3, but computed with the temperature-density relation of models L0.3 (long dashed line), L1 (full line) and L3 (short dashed line). In the hotter models, density peaks are broader, expansion velocities higher and the corresponding absorption features wider.

divergence of the velocity field for the gas at an overdensity ≥ 3 . The distributions shift towards more positive values of $\text{div}_v \cdot v_p$, i.e. a larger fraction of the gas at the center of sheets is expanding, for hotter models. Figure 4, to be discussed in more detail below, shows explicitly for a typical sight line how pressure-induced forces generate peculiar velocities that lead to a smoothing of the gas with respect to the underlying dark matter.

The temperature also affects the normalization constant which determines the mean flux level for a given ionizing background. If the gas distribution were to be independent of temperature, then this constant would simply scale as $T^{-0.7}$ due to the temperature dependence of the recombination coefficient. There is, however, less gas locked in dense regions in the hotter models and consequently the temperature dependence is slightly weaker.

3.1.2 The widths of QSO absorbers

Figure 4 shows the density and velocity fields and the corresponding Ly α spectrum along a typical sight line for different models. Panel (a) shows how a higher temperature leads to broadening of the density peaks in real space. The density peaks in the gas distribution are also significantly broader than in the underlying dark matter due to this Jeans smoothing. Panel (b) shows the corresponding peculiar velocity fields. The gas exhibits significant velocity bias: whereas the dark matter is collapsing towards density peaks, the gas is infalling well away from the central peak but is *expanding* near the density maxima (see also Bryan et al. 1999). Photoheating is in the process of redistributing gas in the shallow potential wells where it collected at higher redshift when the temperature was lower. This effect is obviously stronger for models with a higher heating rate.

The combination of thermal broadening, Jeans smoothing and pressure induced peculiar velocities makes absorption features broader for hotter models, as shown in panel (c). The relative contribution of each of these effects is shown in the final two panels. Panel (d) shows the case where no peculiar velocities are included in the computation of the simulated spectra. Comparing panels (c) and (d) we see that both peculiar velocities and Jeans smoothing are important in determining the shape of the line wings. The wings of lines in model L3 are broader than those for model L0.3 in panel (d) (*without* peculiar velocities). The difference is even greater in panel (c) (i.e. with peculiar velocities). Finally, panel (e) shows spectra for a given density distribution and peculiar velocity field (model L0.3), but with different temperature-density relations imposed. These spectra which now only differ in the amount of thermal broadening look much more similar, but still the shape of the absorption profiles near the peak are more rounded in the hotter models. Note that there are also some differences in the line wings.

3.2 The effect of small scale power

Hui & Rutledge (1999) derived a theoretical expression for the shape of the b -distribution that fits the observations fairly well. They made the *Ansatz* that QSO absorption lines arise from peaks in the density field. Their model explains the observed power law tail of large b -values as being due to the frequent low-curvature fluctuations whereas the sharp cut-off at low b is a consequence of high curvature peaks being exponentially rare. The model also predicts that the widths of the absorption features should depend on the amplitude of the underlying dark matter fluctuations. Models with little small scale power are expected to have on average broader density peaks and hence broader absorption lines.

Figures 4 and 5 demonstrate that the density peaks are indeed wider in the extreme low σ_8 model L1 $\sigma.4$ ($\sigma_8 = 0.4$) than in model L1 ($\sigma_8 = 0.9$, both models have almost identical temperatures). The collapse of the density fluctuations around 100 and 200 km s $^{-1}$ is significantly further advanced in model L1 compared to model L1 $\sigma.4$ and the collapsed structures are much less extended in velocity space. As a result the absorption features in model L1 $\sigma.4$ are much broader than in L1.

However, as is also shown in the figure, the number of Voigt components fitted to the resulting spectra by the Voigt

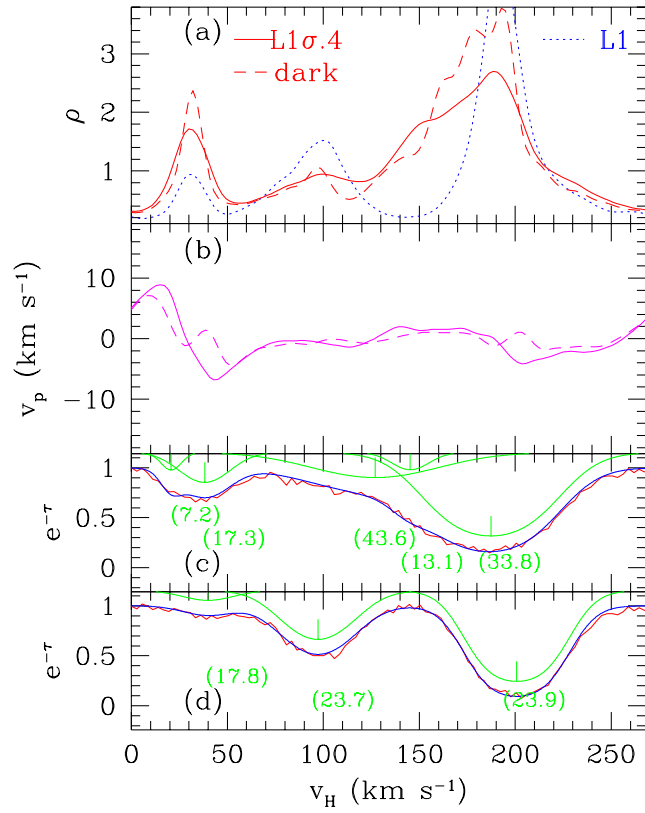


Figure 5. Same sight line as shown in figure 4 for the low fluctuation amplitude model L1 $\sigma.4$. Top two panels show density and peculiar velocity, for the dark matter (dashed line) and gas (full line). The gas density for model L1 is shown dotted in panel (a) for comparison. Panel (c) shows the corresponding fitted spectrum (with noise added, wiggly line), the fit obtained using VPFIT (full line), and the individual Voigt components (full lines with vertical line at maximum absorption), off-set vertically for clarity. The numbers in brackets denote the width of the fitted Voigt profile in km s $^{-1}$ for the lines with $N_{\text{HI}} > 10^{12.4} \text{ cm}^{-2}$. Panel (d) shows the same as panel (c) for model L1.

profile fitting routine VPFIT are different: the spectrum of L1 $\sigma.4$ is fitted with five components while that of L1 is fitted with only three components. It is therefore not obvious that standard Voigt profile fitting routines should require larger b -parameters to fit the more extended density peaks in models with smaller amplitude of dark matter fluctuations where the peaks often show significant substructure. We will show in detail in the next section that this is generally not the case.

4 THE DOPPLER PARAMETER DISTRIBUTION

We compute the Doppler parameters from Voigt profiles fits to absorption features. For both our simulated spectra and the observed spectrum of the $z_{\text{em}} = 3.62$ QSO 1422+231, we use the same automated version of VPFIT.

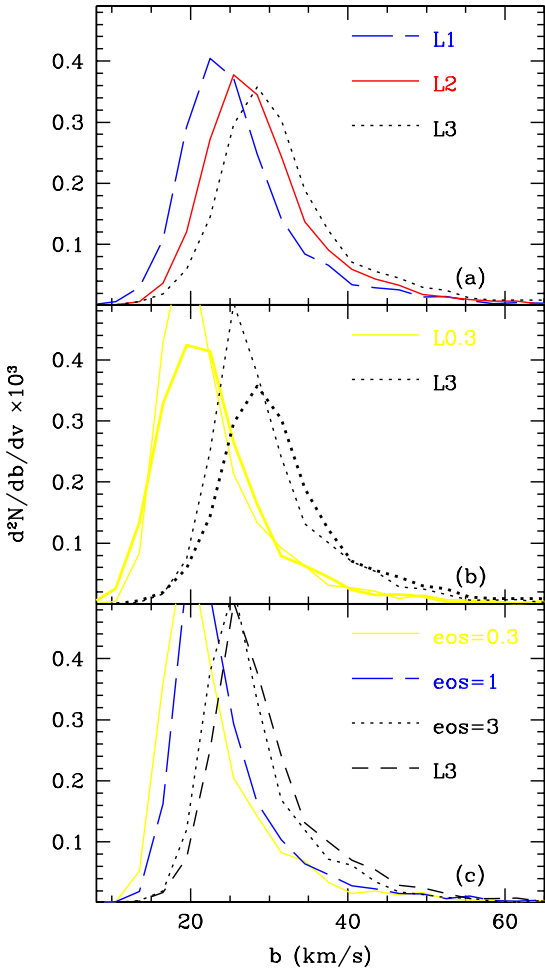


Figure 6. Number of absorption lines per unit width db and per interval dv in Hubble velocity as a function of line width. Included are lines with column density in neutral hydrogen $N_{\text{HI}} > 10^{13} \text{ cm}^{-2}$ for which VPFIT gives an estimated error in b , $b_{\text{err}} < 0.25b$. Panel (a) compares models with increased helium heating L1-L3. Panel (b) compares models L0.3 and L3 with (thick lines) and without (thin lines) peculiar velocities. Finally, panel (c) compares model L0.3 without peculiar velocities with the temperature-density relations of model L0.3, L1 and L3 imposed. Model L3, without peculiar velocities, is shown as the short dashed line.

4.1 The global shift of the distribution with temperature

The general shape of the b -parameter distribution is rather skewed, with a slow fall off in the number of lines larger than the mode, but a rapid drop in the fraction of lines narrower than the mode. We will refer to the position at small b where the fraction of lines starts dropping rapidly as the ‘cut-off’. (A more rigorous definition is possible (Schaye et al. 1999a) but here we will only compare b -distributions between different models and so we do not need a more accurate definition of cut-off, since the differences amongst the models are relatively large anyway.)

The effect of increased heating on the b -parameter dis-

tribution is shown in figure 6a. Increasing the helium heating rate (models L1 to L3) shifts the cut-off in narrow lines from $\leq 20 \text{ km s}^{-1}$ to $\geq 25 \text{ km s}^{-1}$ and decreases the fraction of lines at the peak. In addition to that, the hotter model L3 has significantly more broad lines with $b \geq 40 \text{ km s}^{-1}$ than L1. Note that we have not normalized the distributions to demonstrate that the increase in broad lines is not due to a decrease in the number of narrow lines. As discussed in the previous section, the global shift is due to the combined effect of Jeans smoothing, pressure-induced peculiar velocities and thermal broadening.

The effect of peculiar velocities on the Doppler parameter distribution has been controversial and both a narrowing and broadening has been claimed. Figure 6b compares the line-widths distribution for models L0.3 and L3 with and without peculiar velocities. The effects of peculiar velocities are more pronounced for the hotter model L3. Peculiar velocities broaden the absorption lines and also significantly decrease the number of lines around the maximum in the distribution. This behaviour can be understood by looking again at figure 4, which shows that pressure-induced peculiar velocities tend to oppose the infall into sheets, and this effect is larger for the hotter model. Consequently, peculiar velocities do not change the distribution of b -parameters very much in the cold model while in the hot model the absorption lines become broader.

Note that these pressure induced peculiar velocities are not due to shocking of the gas: the higher temperatures are purely a result of increased photo-heating. It is photo-heating that drives the higher density gas into its lower density surroundings, which results in the changes in the density and velocity divergence PDFs shown earlier. The high density gas collected at the bottom of the dark matter potential wells at higher redshifts, when the heating rates were lower and the gas was colder.

To illustrate the effect of pure thermal broadening, we have computed spectra from the numerical simulations after having artificially changed the temperature-density relation of the gas. The resulting Doppler parameters for model L0.3, without peculiar velocity contributions, and with the temperature-density relations of model L0.3, L1 and L3 imposed are shown in Figure 6c. Increasing the amount of thermal broadening shifts the cut-off at small b to larger values. The position of the cut-off is thus a measure of the temperature of the gas. This is at the heart of the method developed by Schaye et al. (1999a), who used numerical simulations to demonstrate that the IGM temperature can be measured to high accuracy by comparing the lower cut-off of the Doppler parameter distribution of simulated spectra to that of the observed distribution. Comparing the full line with the dotted line shows that with increased thermal broadening the number of broad lines increases as well.

The effect of Jeans smoothing can be seen by comparing the dotted with the short dashed lines. Both these models are with peculiar velocities set to zero and with the $T - \rho$ relation of model L3, but the first uses the density distribution of L0.3 and the second the one of L3. The extra broadening of the lines is thus purely due to the widening of the absorbers in real space, due to the increased pressure gradients in the hotter model. The wider structures have an increased differential Hubble flow resulting in wider absorp-

tion lines. Note that the magnitude of this effect is smaller than that of thermal broadening.

4.2 The effect of small scale power

In section 3.2 we showed that models with less small scale power have significantly wider absorption features. The effect of this widening on the b -distribution (i.e., the probability distribution of lines as a function of their width, here for lines with $N_{\text{HI}} \geq 10^{13} \text{ cm}^{-2}$) is shown in figure 7, which compares models L1 and L1 σ .4, which have the same $T - \rho$ relation, but different values of σ_8 . The two models have almost identical b -parameter distributions, which can be understood as follows. When fitting a Voigt profile to a relatively broad absorption feature with a non-Voigt shape, as often occurs for models where the broadening is not thermally dominated, there is a trade-off between fitting a single broad Voigt line (which might not fit particularly well) or fitting multiple narrower lines. VPFIT was developed to ‘deblend’ absorption features into thermally broadened Voigt profiles and generally selects the option of fitting more but narrower lines with thermal shapes. Therefore, even for the wide absorption features in model L1 σ .4 the widths of the fitted Voigt profiles are still closely related to their “thermal” width. The b -distribution for models L1 and L1 σ .4 are thus very similar, since they have the same temperature.

We have fitted the two models with different σ_8 with another Voigt profile fitting routine, AUTOVP, kindly provided to us by Romeel Davé (Davé et al. 1997) to check if this result is special to VPFIT. The b -distribution obtained with AUTOVP is very similar to that obtained with VPFIT, in particular, there is no strong dependence of the b -distribution on the amplitude of the dark matter fluctuations. This result contrasts with the findings of Bryan & Machacek (1999), who did find a strong dependence of the b -distribution on σ_8 using different profile fitting software.

Finally, we confirm the result of Gnedin (1998) that changing the amplitude of dark matter fluctuations affects the column density distribution as shown in figure 8. At low column densities this is because many more weak lines are now required to fit the broader features. At the same time, L1 σ .4 has fewer strong lines and so the column density distribution steepens with decreasing σ_8 .

4.3 Comparison to the observed Doppler parameter distribution

Figure 9 compares the Doppler parameter distribution of some of our models to the observed distribution for QSO 1422+231. We have fitted the Ly α spectrum of this QSO using our automated version of VPFIT, thereby analysing observed and simulated spectra in the same way. We plot the b -distribution of the fitted lines for the top and bottom half of the spectrum separately.

Model L1 reproduces the observed b -distribution of the top half of QSO 1422+231 reasonably well, providing a good fit to both the cut-off at small b , and to the tail of broader lines with $b \geq 40 \text{ km s}^{-1}$. However for the lower redshift half, L1 seems to cut-off at too small values of b , and in addition fails to reproduce the observed number of broader lines. Interestingly, the hotter model L2 *does* provide a good

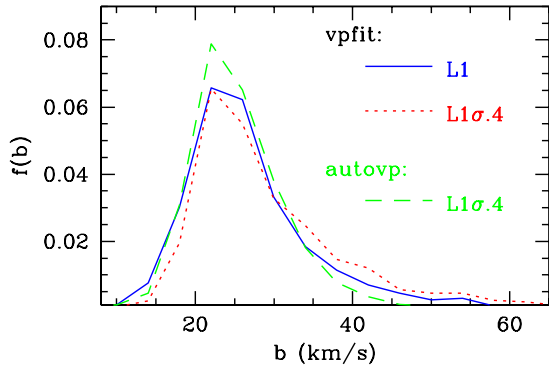


Figure 7. Fraction of lines with a given width, $f(b)$, for models L1 (full line) and L1 σ .4 fitted with VPFIT (dotted line) and using AUTOVP (dashed line). Although the structures in the extreme low σ_8 model are significantly broader than in L1, this is not reflected in the b -distribution. The b -distributions obtained using VPFIT and AUTOVP are very similar.

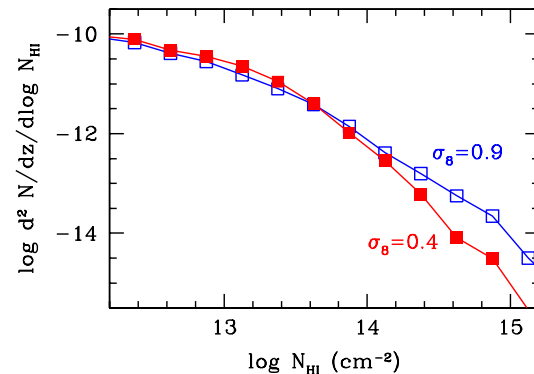


Figure 8. Column density distribution for model L1 (open squares) compared to L1 σ .4 (filled squares). The low normalization model has significantly less high column density systems.

fit to the bottom half of QSO 1422+231 over the whole b range. A more thorough investigation (Schaye et al. 1999b) demonstrates that the low redshift half of QSO 1422+231 is indeed hotter.

Turning our attention to a comparison between the different models, we see that models L1 and LX produce very similar b -distributions. Compton heating by the hard X-ray background is not able to raise the temperature of the gas probed by these lines significantly above the value which results from helium photoheating as computed by Haardt & Madau (1996). However there is a significant difference in temperature in regions of very low densities between L1 and LX, which might be measurable with other flux statistics. Finally, models L2 and S3 also have very similar b -distributions. Both models have a temperature of $\gtrsim 15000 \text{ K}$ at mean density. In the standard CDM model S3 ($\Omega_m = 1$), the adiabatic cooling time scale is smaller than in the Λ CDM model ($\Omega_m = 0.3$, $\Omega_\Lambda = 0.7$). This explains why the Doppler parameter distribution are similar despite the larger HeII heating rate in model S3.

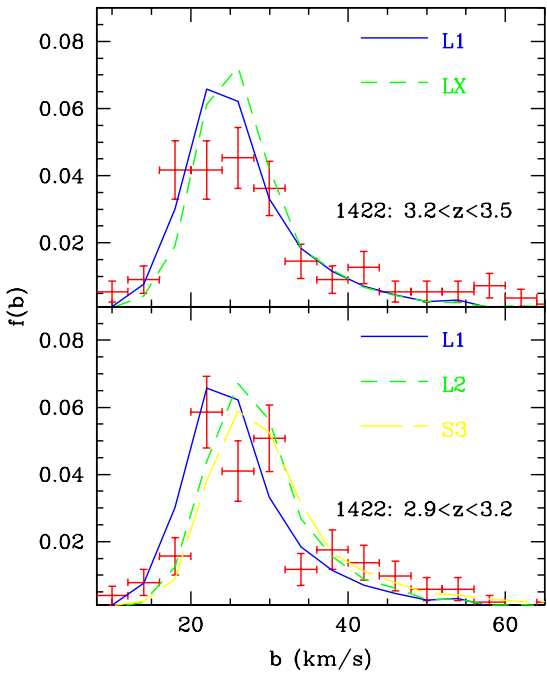


Figure 9. Fraction of lines with a given width, $f(b)$, versus b for lines with $N_{\text{HI}} > 10^{13} \text{ cm}^{-2}$ with formal errors $b_{\text{err}} \leq 0.25b$, obtained from VPFIT. Symbols with (Poissonian) error bars are from fitting the spectrum of QSO 1422+231 using our automated version of VPFIT, which produced ~ 350 lines that met our selection criterion. Top (bottom) panel contains the top (bottom) half of the observed spectrum, the corresponding redshift ranges are indicated. The top panel compares the data to models L1 and LX, the bottom panel to L1, L2 and S3. L1 reproduces the observed distribution well for the top half of QSO 1422+231, but the bottom half seems to be fit better by L2. Models L1 and LX are very similar, as are models L2 and S3.

5 OTHER FLUX STATISTICS

In this section we investigate the effect of the thermal broadening mechanism and that of the amplitude of dark matter fluctuations on small scales on the one- and two-point functions of the flux and on the flux power spectrum. These statistics are in principle easier to compute than the b -distribution but are likely to be affected by a number of observational biases. For example, Rauch et al. (1997) showed that the shape of the one-point function (flux probability distribution) evolves strongly with redshift, as a consequence of the rapid evolution of the effective optical depth. Therefore, given that a QSO spectrum spans a relative large redshift range, such evolution should be accounted for in a comparison with simulations. We have followed the procedure described in detail in Section 2 to compare our simulations to the spectral statistics of QSO 1422+231.

5.1 The one-point function of the flux

The shape of the one-point function depends strongly on the assumed mean absorption, the continuum fit, and on the noise properties. For example, figure 10a shows the dif-

ferences between the top and bottom halves of the Ly α spectrum of QSO 1422+231 due to redshift evolution of the mean absorption, cosmic variance, and non-uniform signal to noise over the spectrum.

The importance of using the correct noise properties is illustrated in figure 10b where we compare the one-point function for a simulated spectrum with Gaussian noise independent of flux (dotted line) and with the more elaborate method described in Section 2 (short dashed line). There are significant differences, especially for saturated pixels ($F = 0$). Adding noise broadens the peak around nearly saturated pixels considerably compared to the case where the noise properties are similar to that in the observed spectra. In addition, a relatively large fraction of the pixels around $F = 0$ comes from a few rare high column density systems. To test this we have removed the four highest column density systems from the spectrum of Q1422 (column densities between $10^{15.2}$ and $10^{17.9} \text{ cm}^{-2}$) and recomputed the one-point function. These two functions now differ significantly around $F = 0$. Since such strong systems are relatively rare, the shape of the one-point function round $F = 0$ suffers from small number statistics.

For the full curve in figure 10b the spectra were calculated as before but we have now also continuum fitted the simulated spectra as described in Theuns et al. (1998). Comparing the short dashed line with the full line shows that, not surprisingly, continuum fitting has a big effect on the shape of the one-point function around $F = 1$. The smallness of our simulation box probably exacerbates this problem but it should be kept in mind that the continuum level of observed QSOs is often rather ill defined, especially at higher z . In the remainder of this section, we will present one-point functions computed using the noise properties of QSO 1422, and including continuum fitting. Finally, figure 10c compares models L3 and L3b: missing large scale power has a relatively significant effect on the one-point function, but this should not limit comparison between different models.

Figure 11a compares the one-point function for the cold model L0.3 to the hot model L3. The trend is as expected: the cold model has relatively more pixels round $F \sim 0.1$, since a larger fraction of the colder gas has collapsed to higher densities, but less absorption around $0.2 \leq F \leq 0.7$, since the hotter model is denser in the regions surrounding dense peaks. This is due to the increased pressure forces in the hotter model driving more of the gas out of the centres of potential wells into the lower density regions. The middle panel shows that the effect of less small scale power is similar to that of higher temperatures: L1 $\sigma.65$ has fewer pixels round $F = 0$ but more absorption in the low density regions around $0.2 \leq F \leq 0.7$. Because of the difference in power, gas in L1 $\sigma.65$ is less collapsed in high density regions, and so there is correspondingly more gas in lower density regions to boost the one-point function in the region $0.2 \leq F \leq 0.7$. Machacek et al. (1999) also showed that the shape of the optical depth distribution is a sensitive probe of the amplitude of density fluctuations on small scales. However, as we have just demonstrated, the effect of temperature on the flux decrement distribution and that of the fluctuation amplitude of the DM density are largely degenerate. Finally, figure 11c shows that model L3b reproduces the observed one-point function reasonably well.

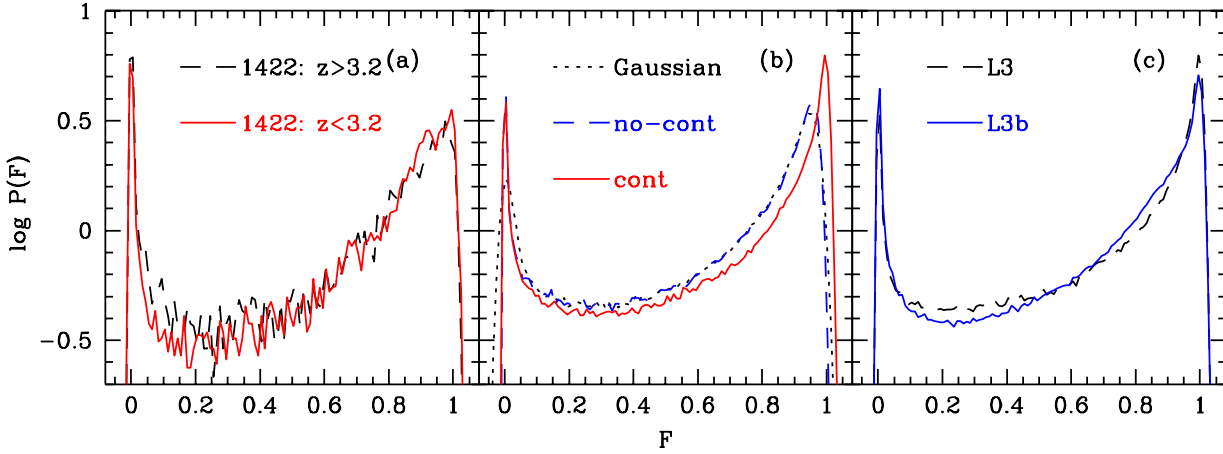


Figure 10. One-point function of the flux. Panel (a): comparison of top half of the Ly α forest of QSO 1422+231 (dashed line) with the bottom half (full line). Cosmic variance, optical depth evolution and varying signal to noise are responsible for the differences. Panel (b): simulated spectra at the corresponding redshift, assuming Gaussian noise with effective signal-to-noise of 50 and no continuum fitting (dotted line) and using the noise properties of QSO 1422+231 without (short dashed line) and with (full line) continuum fitting. Continuum fitting affects the high end significantly, whereas the noise properties are important at low flux levels. Panel (c): comparison of models L3 (dashed line) and L3b (full line) illustrating the effect of missing large scale power.

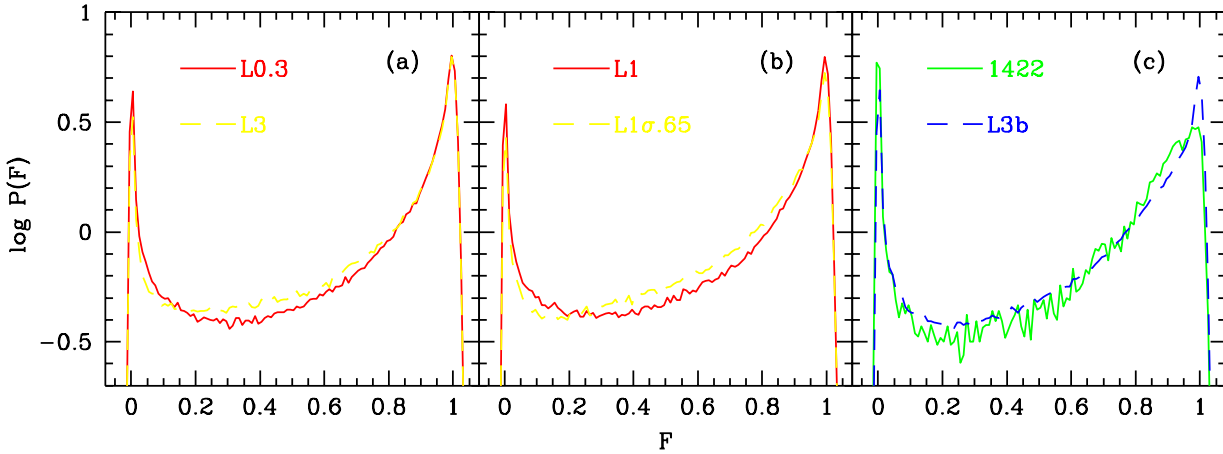


Figure 11. Comparison between one-point functions. In panel (a) model L0.3 (full line) versus L3 (dashed line); in panel (b): model L1 (full line) versus model L1 σ .65 (dashed line); in panel (c) model L3b (dashed line) versus QSO 1422+231 (full line). Increasing temperature has the same effect as decreasing σ_8 . Model L3b reproduces the observed one-point function reasonably well.

5.2 The two-point function of the flux

The two-point function of the flux, $P(F_1, F_2, \Delta v)$, is the probability that two randomly chosen pixels separated by a velocity interval Δv will have transmitted fluxes F_1 and F_2 (Miralda-Escudé et al. 1997). A convenient way of visualizing this function is by considering the mean flux difference for F_1 in a given flux interval, that is, select a flux interval δF_1 and consider the mean flux difference

$$\overline{\Delta F}(v; \delta F_1) \equiv \int_{\delta F_1} \left\{ \int_{-\infty}^{+\infty} (F_1 - F_2) P(F_1, F_2, \Delta v) dF_2 \right\} dF_1 / \delta F_1 \quad (2)$$

The shape of $\overline{\Delta F}(v; \delta F_1)$ contains information on the profile of the absorbers, or in the traditional language, on the widths of the lines. For large velocity differences, the correlation between the pixels is lost and the two-point function contains no extra information over the one-point function. In this limit, the mean flux difference will tend to the mean flux minus the mean flux of the pixels in the flux interval under consideration. Since $\overline{\Delta F}$ is an averaged quantity, the interpretation of the two-point function is not always obvious.

Figure 12 compares the two-point function for several models and for QSO 1422 and for two flux intervals,

$-0.05 \leq F_1 \leq 0.05$ (flux class 1) and $0.05 \leq F_1 \leq 0.15$ (class 2). The temperature of the gas is clearly important: the two-point function shows that pixels are correlated over larger scales for hotter models, as expected given the broadening of absorption lines with increasing temperature. As with the one-point function, there is also a rather important effect of missing long waves in our small simulation boxes. The effect of small scale power on the other hand is surprisingly small, the two-point functions of models L1 and $L1\sigma.65$ are almost indistinguishable. Only for model $L1\sigma.4$ which has very much less small scale power are the differences significant. This is mostly due the much lower number of high column density absorbers in this low normalization model.

Model L3b reproduces the two-point function of QSO 1422 up to 30km s^{-1} , but then appears less correlated for larger velocity differences than the data. Unfortunately, just as for the one-point function, flux class 1 is relatively strongly influenced by the presence of a few strong absorbers in the data (compare the dashed with the dotted line). The relatively good correspondence between model L3b and the data suggests that the temperature of the IGM at mean density is high, $\gtrsim 15000\text{K}$ at this redshift.

5.3 Flux power spectrum

We begin by discussing the relation between the flux power spectrum and the underlying spectrum of density fluctuations. For a Gaussian random field, the power spectrum of density fluctuations along a sight line, $P_{1D}(k)$, is defined as the ensemble average of the square of the Fourier transform of the density $\rho(v)$,

$$\delta_\rho(k) = \int_0^V \rho(v) \exp(-ikv) dv / \langle \rho \rangle, \quad (3)$$

where V is the length of the sight line, and ρ is the density as function of the Hubble velocity v . It is related to the three dimensional power spectrum of the field, $P_{3D}(|\mathbf{k}|)$, through an integration (Kaiser & Peacock 1991)

$$P_{1D}(k) = \frac{1}{2\pi} \int_k^\infty P_{3D}(q) q dq. \quad (4)$$

This equation shows that $P_{1D}(k)$ has contributions from all waves with $q > k$. Since Jeans smoothing introduces a small-scale cut-off in the power spectrum of the three dimensional density field, it influences $P_{1D}(k)$ for the gas on all scales.

The observed flux is related to the gas density in redshift space by the relation

$$F = \exp[-\mathcal{A}(\rho_{\text{gas}} / \langle \rho_{\text{gas}} \rangle)^\alpha], \quad (5)$$

and the flux power spectrum $P_F(k)$ is defined as the ensemble average of the square of the Fourier transform of $F(v)$,

$$\delta_F(k) = \int_0^V F(v) \exp(-ikv) dv. \quad (6)$$

Peculiar velocities and thermal broadening contribute to the small scale cut-off of $P_F(k)$. The factor \mathcal{A} ($\propto A$) in equation 5 is a normalization constant that determines the mean flux, and acts as a ‘bias’ factor between density and flux. The exponent α depends on the slope of the $\rho-T$ relation. $P_F(k)$ differs from $P_{1D}(k)$ due to the combined effects

of Jeans smoothing, redshift space distortions and thermal broadening, and in addition due to the non-linear relation 5.

Figure 13 compares $k P_F(k)$ for several models and for QSO 1422+231. On small scales still above the resolution limit in the dark matter, the power spectrum dependence $P_{3D} \sim k^{-3}$ implies that $k P_{1D}(k)$ depends only weakly on k , highlighting that the observed sharp cut-off in $k P_F(k)$ is due to thermal smoothing. To compute these power spectra, we performed the following steps. The simulated spectra were calculated in the same way as we before, i.e., scaling the models to the same mean flux, and adding noise with the same properties as that of the spectrum of QSO 1422. We have chosen a somewhat smaller pixel size of 2.2km s^{-1} to facilitate the use of a fast Fourier transform routine to calculate $P_F(k)$. To calculate the power spectrum of the observed spectrum, we re-sampled the spectrum to the same pixel size as the simulated spectra and divided it into stretches with lengths equal to that of our simulated spectra. We took care to use stretches that have a flux close to one at the edges and in addition multiplied the flux with a windowing function, in order to be able to use ‘periodic’ boundary conditions in the FFT. We then computed the Fourier transform for each stretch separately and averaged the power per mode. To estimate the influence of missing large scale power in our small simulation boxes, we compare models L3 and L3b, which are identical except for the size of the simulated region. As we show below, the differences in the flux power spectrum between these models is very small.

On large scales where gas follows dark matter, equations 4 and 5 can be combined to infer the three dimensional power spectrum from the flux power spectrum (Croft et al. 1997). In contrast, on small scales, $\log k (\text{km}^{-1} \text{s}) \geq -1.4$, thermal smoothing strongly suppresses the amplitude of $P_F(k)$. Panel (a) demonstrates how this cut-off moves to smaller wavenumbers for higher temperatures. The solid curve is for the cold model L0.3 while the dashed curve is for the hot model L3. The dotted curve is for the larger box L3b and there is a hint of increased power on the largest scales but the effect seems to be small.

Panel (b) shows that there is little dependence of the small scale flux power spectrum on σ_8 . This may seem surprising at first but is largely due to the fact that we have rescaled all simulated spectra to the observed mean flux (see Croft et al. 1997 for a discussion of this point). The dot-dashed line is for model $L1\sigma.4$, but imposing the same normalization A as for model L1, thereby increasing the effective optical depth from $\sim .33$ to $\sim .43$. The power spectrum for this model now differs significantly from the others. Consequently, scaling models to the same mean flux removes most of the dependence of the flux power spectrum on the fluctuation amplitude of the DM distribution on these small scales. Given that the shape of $P_F(k)$ depends strongly on temperature suggests it can be used as an independent method to measure the temperature of the IGM.

Panel (c) compares L3b to the observed spectrum of QSO 1422. The full line shows $k P_F(k)$ for L3b but without adding noise to the spectra. Comparison to the dashed line shows that the shape of $P_F(k)$ for $\log k (\text{km}^{-1} \text{s}) \geq -0.5$ is set by the noise properties. Imposing the noise of QSO 1422 onto our hot model L3b gives a simulated power spectrum in excellent agreement with that of 1422. Therefore, both the two-point function and the flux power spectrum on small

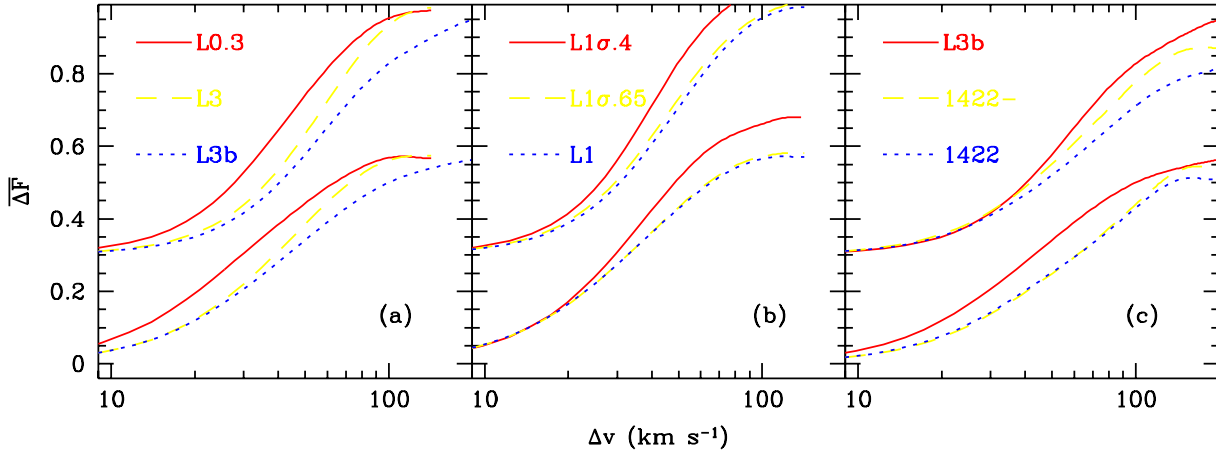


Figure 12. Two-point functions for several models and for QSO 1422+231 for flux class 1 ($-0.05 < F_1 < 0.05$) and flux class 2 ($0.05 < F_1 < 0.15$). Panel (a): models L0.3 (full line), L3 (dashed line) and L3b (dotted line). Top curves are for class 1 and are off-set vertically by 0.3. Panel (b) is the same as (a) but for models L1 σ .4 (full line), L1 σ .65 (dashed line) and L1 (dotted line). Panel (c) is the same as panel (a) but for model L3b (full line), QSO 1422 with the four strongest lines removed (dashed line) and QSO 1422 (dotted line). Panel (a) shows that temperature and box size have an important effect on the two-point function, in contrast to the amount of small scale power (panel b). There are significant differences between the simulated and observed two-point functions, but these are at least partly due to missing large scale power in the simulations (panel a), and to strong absorbers in the observations (panel c).

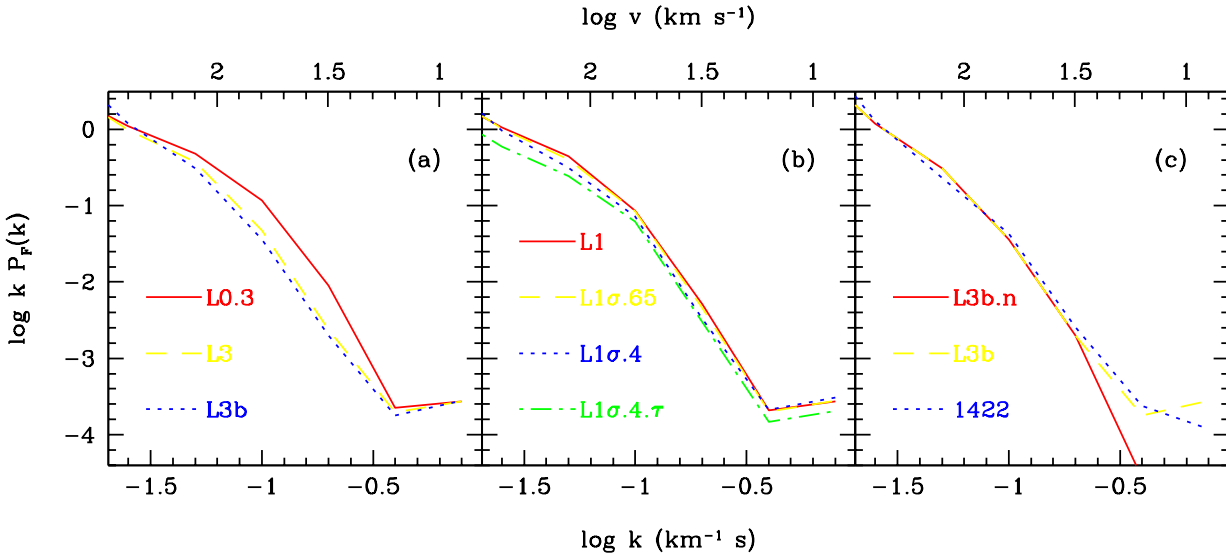


Figure 13. Flux power spectrum for several models and for QSO 1422+231. Panel (a): models L0.3 (full line), L3 (dashed line) and L3b (dotted line); panel (b): models L1 (full line), L1 σ .65 (dashed line) and L1 σ .4 (dotted line). Model L1 σ .4 but with the same ionizing background as L1 (same factor A , see table 1) is shown with the dot-dashed line. Panel (c) shows models L3b without (full line) and with noise (dashed line), and QSO 1422 (dotted line). The bottom axes refer to wave number k , the top axes to the corresponding Hubble velocity $v = 2\pi/k$. Panel (a) shows that temperature has an important influence on the shape of $P_F(k)$, and that the effect of missing long waves is small. Panel (b) shows that σ_8 has relatively little effect, if models are compared at the same mean flux. Panel (c) shows that the shape of $P_F(k)$ for $k \geq -0.7$ is set by the noise, and that L3b fits the power spectrum of QSO 1422 on small scales very well.

scales suggest that the IGM temperature at $z \sim 3.25$ is high, $\gtrsim 15000$ K.

6 DISCUSSION AND CONCLUSIONS

We have used numerical simulations to investigate what determines the widths of Ly α absorbers in QSO spectra. These

absorbers arise when a line of sight intersects a peak in the neutral hydrogen density, which itself is due to gas falling into the sheet-like and filamentary potential wells of the underlying dark matter distribution. The widths of the absorbers are set by two very different processes. Firstly, the amount of small scale power determines the widths of the dark matter potential wells. Secondly, Jeans smoothing of the gas due to its high temperature ensures it is distributed

much smoother than the dark matter on small scales. Finally, the corresponding absorption features are wider than the absorbers in real space due to peculiar velocities and thermal broadening.

The strong dependence on the amount of small scale power is due to the fact that the linearly extrapolated fluctuation amplitude on the Jeans scale is of order unity for the models of interest. For this reason, the collapse of structures on scales comparable to the Jeans length is less advanced in models with a lower amplitude of DM fluctuations.

The effect of temperature on the widths of peaks in the gas distribution can be understood as follows. Larger temperature gradients between high and low density regions, as occur in hotter models, lead to increased pressure gradients that push gas out into the wings of the underlying dark matter potential wells. Consequently, less gas collapses into high density regions and voids in the density distribution become less underdense, making the peaks wider. This smoothing process is particularly efficient for photoionized gas because it obeys a temperature-density relation where the gas temperature increases with density, and this increases the pressure gradient over its isothermal value.

We have further investigated what effect the different broadening mechanisms have on the resulting absorption spectra. We used the Doppler parameter distribution as obtained with the standard Voigt-profile fitting routines VPFIT and AUTOVP, the one- and two-point functions of the flux, and the flux power spectrum to characterize the absorption spectra.

The Doppler parameter distribution is mainly determined by the combined effect of the three thermal smoothing mechanisms, thermal broadening, thermally driven peculiar velocities and Jeans smoothing. It shows little dependence on the amplitude of dark matter fluctuations. VPFIT and AUTOVP are therefore rather successful in deblending absorption features into thermally broadened Voigt profiles. Individual Voigt components often trace the substructure in broader density peaks. This is the reason why the Doppler parameter distribution shows little sensitivity to the overall width of the density peaks, which themselves depend strongly on the amplitude of dark matter fluctuations.

The flux two-point function and the flux power spectrum on small scales are also mainly determined by thermal broadening and show likewise no strong dependence on the amplitude of dark matter fluctuations. This is at least partially due to the fact that we have chosen to scale our simulated spectra to match the mean observed flux. The one-point function of the flux, however, depends on temperature and normalization of the DM fluctuation amplitude in a similar way. This degeneracy arises because the PDF of the density depends mainly on the *rms* fluctuation amplitude of the gas, which itself depends on both the fluctuation amplitude of the DM density and on the scale on which the gas distribution is smoothed relative to the DM distribution.

We conclude that the Doppler parameter distribution, the flux two-point correlation function and the flux power spectrum on small scales are sensitive probes of the temperature of the photoionized IGM, while the one-point function of the flux can be used to probe the fluctuation amplitude on small scales once the temperature is known.

When comparing our simulated spectra with a high resolution spectrum of QSO 1422+231, obtained with the

HIRES spectrograph on the Keck telescope, we find that the Doppler parameter distribution, the two-point correlation function and the flux power spectrum are best matched by models that have a temperature of the IGM of $\gtrsim 15000\text{K}$ at mean density at $z = 3.25$. This temperature is ~ 50 per cent higher than in our reference model L1 that used the heating rates calculated for the Haardt & Madau spectrum. (Note however, that in this paper we have only varied the amplitude of the $\rho - T$ relation, and not its slope. This prevents us from making stronger statements about the value of T_0 .) The flux one-point function depends both on temperature and the level of small scale fluctuations. A ΛCDM model with this temperature matches the observed one-point function reasonably well. Once an accurate measurement of T_0 is available, it should be possible to determine σ_8 accurately from the Ly α forest.

ACKNOWLEDGMENTS

We thank M. Rauch and W. Sargent for providing us with the HIRES spectrum of the QSO 1422+231. JS thanks the Isaac Newton Trust, St. John's College and PPARC for support. We thank R. Carswell for helping us with VPFIT. This work has been supported by the 'Formation and Evolution of Galaxies' network set up by the European Commission under contract ERB FMRX-CT96086 of its TMR programme. Research conducted in cooperation with Silicon Graphics/Cray Research utilising the Origin 2000 supercomputer at DAMTP, Cambridge.

REFERENCES

- Abel T., Haehnelt M., 1999, ApJL, 520, L13
- Bahcall J.N., Salpeter E.E., 1965, ApJ, 142, 1677
- Bryan G.L., Machacek M., Anninos P., Norman M.L., 1999, ApJ, 517, 13
- Bryan G.L., Machacek M.E., 1999, preprint (astro-ph/9906459)
- Bond J.R., Kofman L., Pogosyan D., 1996, Nature, 380, 603
- Burles S., Tytler D., 1998, ApJ, 499, 699
- Carswell R.F., Webb J.K., Baldwin J.A., Atwood B., 1987, ApJ, 319, 709
- Cen R., 1992, ApJS, 78, 341
- Cen R., Miralda-Escudé J., Ostriker J.P., Rauch M., 1994, ApJL, 437, L9
- Couchman H.M.P., 1991, ApJL, 368, L23
- Couchman H.M.P., Thomas P.A., Pearce F.R., 1995, ApJ, 452, 797
- Croft R., Weinberg D.H., Katz N., Hernquist L., 1997, ApJ, 488, 532
- Davé R., Hernquist L., Weinberg D.H., Katz N., 1997, ApJ, 477, 21
- Efstathiou G., Bridle S.L., Lasenby A.N., Hobson M.P., Ellis R.S., 1999, MNRAS in press (astro-ph/9812226)
- Eke V.R., Cole S., Frenk C.S., 1996, MNRAS, 282, 263
- Freedman J.B., Mould J.R., Kennicutt R.C., Madore B.F., 1998, preprint (astro-ph/9801080)
- Gingold R.A., Monaghan J.J., 1977, MNRAS, 181, 375
- Gnedin N.Y., 1998, MNRAS, 299, 392
- Gunn J.E., Peterson B.A., 1965, ApJ, 142, 1633
- Haardt F., Madau P., 1996, ApJ, 461, 20
- Haehnelt M.G., Steinmetz M., 1998, MNRAS, 298, 21
- Hernquist L., Katz N., Weinberg D.H., Miralda-Escudé J., 1996, ApJL, 457, L51

- Hui L., 1999, in proceedings of ESO/MPA conference Evolution of Large Scale Structure, eds. A. Banday, R. Sheth, L. Da Costa
- Hui L., Gnedin N.Y., 1997, MNRAS, 292, 27
- Hui L., Rutledge R.E., 1999, ApJ, 517, 541
- Kaiser N., Peacock J., 1991, ApJ, 379, 482
- Lucy L.B., 1977, AJ, 82, 1023
- Machacek M.E., Bryan G.L., Meiksin A., Anninos P., Thayer D., Norman M.L., Zhang Y., 1999, preprint (astro-ph/9906297)
- Madau P., Estahou G., 1999, ApJL, 517, L9
- Miralda-Escudé J., Rees M., 1994, MNRAS, 266, 343
- Miralda-Escudé J., Cen R., Ostriker J.P., Rauch M., 1996, ApJ, 471, 582
- Miralda-Escudé J., et al., 1997, to appear in Proceedings of 13th IAP Colloquium: Structure and Evolution of the IGM from QSO Absorption Line Systems, eds. P. Petitjean, S. Charlot
- Nath B.B., Sethi S.K., Shchekinov Y., 1999, MNRAS, 303, 1
- Hui L., Rutledge R.E., 1999, ApJ, 517, 541
- Rauch M., Miralda-Escudé J., Sargent W.L.W., Barlow T.A., Weinberg D.H., Hernquist L., Katz N., Cen R., Ostriker J., 1997, ApJ, 489, 7
- Seljak U., Zaldarriaga M., 1996, ApJ, 469, 437
- Schaye J., Theuns T., Leonard A., Efstathiou G., 1999a, MNRAS, 310, 57
- Schaye J., Theuns T., Rauch M., Efstathiou G., Sargent W.L.W., 1999b, submitted
- Theuns T., Leonard A., Efstathiou G., Pearce F.R., Thomas P.A., 1998, MNRAS, 301, 478
- Theuns T., Leonard A., Schaye J., Efstathiou G., 1999, MNRAS 303, L58
- Wadsley J., Bond J.R., 1996, in "Computational Astrophysics", Proc. 12th Kingston Conference, Halifax, Oct. 1996, ed. D. Clarke & M. West (PASP)
- Zhang Y., Anninos P., Norman M.L., 1995, ApJL, 453, L57
- Zhang Y., Anninos P., Norman M.L., Meiksin, A., 1997, ApJ, 485, 496